Applied Surface Science 679 (2025) 161214

Contents lists available at ScienceDirect

Applied Surface Science

journal homepage: www.elsevier.com/locate/apsusc

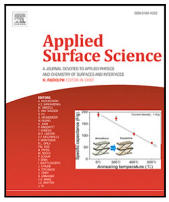

Full length article

Laser engineered architectures for magnetic flux manipulation on superconducting Nb thin films

Elena Martínez [a,1], Nicolas Lejeune [b,1], Javier Frechilla [a], Luis Porta-Velilla [a], Emile Fourneau [b], Luis A. Angurel [a], Germán F. de la Fuente [a], Jörn Bonse [c], Alejandro V. Silhanek [b], Antonio Badía-Majós [a,*]

[a] Instituto de Nanociencia y Materiales de Aragón (INMA), CSIC-Universidad de Zaragoza, Zaragoza, Spain
[b] Experimental Physics of Nanostructured Materials, Q-MAT, CESAM, Université de Liège, Liège, Belgium
[c] Bundesanstalt für Materialforschung und –prüfung (BAM), Berlin, Germany

ARTICLE INFO

Dataset link: https://doi.org/10.5281/zenodo.11521075

Keywords:
Laser-induced periodic surface structures (LIPSS)
Magnetic flux
Magneto-optical imaging (MOI)
Critical current density

ABSTRACT

Custom shaped magnetic flux guiding channels have been fabricated on superconducting Nb thin films by laser nanopatterning of their surface. Preferential pathways are defined by suitable combination of imprinted anisotropic pinning domains through laser-induced periodic surface structures (LIPSS). Generated by the selective energy deposition of femtosecond UV laser pulses, quasi-parallel ripple structures are formed under optimized irradiation conditions. On average, each domain is formed by grooves with a lateral period of 260–270 nm and a depth about 80 nm. By combination of scanning and transmission electron microscopy, magneto-optical imaging, and conductive atomic force microscopy techniques, we conclude that the boundaries of the LIPSS-covered domains play a prominent role in the magnetic flux diversion process within the film. This is confirmed by dedicated modeling of the flux dynamics, combined with the inversion of the magneto-optical signal. The created metasurfaces enable control of the flux penetration process at the microscale.

1. Introduction

The manipulation of electromagnetic (EM) fields plays a prominent role in the development of cutting-edge technologies, in particular within the field of microelectronics. Of special mention are the superconducting circuits for quantum computation and magnetic sensing [1,2], the nano-magnet based logical circuits [3,4], and the so-called fluxonic devices [5–8], that may host conceptual breakthroughs in computer engineering. Switching the system from one state to another and reaching enough sensitivity require control of the applied magnetic fields in the submicron scale, a target that may be achieved by superconducting nanoarchitectures. Although all these applications take advantage of many properties related to the superconducting state (zero dissipation, fast switching velocities, magnetic flux quantization), one must also face a variety of shortcomings. In particular, let us mention that the nucleation of quantized magnetic flux units (vortices) [9] may become highly detrimental when they penetrate in the form of catastrophic flux avalanches. This has been observed in superconducting radio frequency resonators [10,11], when they are used as readout devices in qubit computing systems. Other issues to be accounted for relate to geometrical effects, highly relevant due to the quasi-2D nature of the integrated technologies. Thus, finite size effects with the concomitant demagnetizing fields or the rapid spreadout of field with distance require dedicated consideration if either field concentration or shielding in a targeted area is to be achieved.

Focused on superconducting technologies, the idea of guiding magnetic fields by using artificial structures acting as flux rails comes from aged contributions [12–15] showing that, in thin samples, perpendicular magnetic flux vortices tend to be guided along microstructural features such as grooves in grated structures. Characteristic grating (line separation and depth) must be in the submicron scale, since the basic underlying physical principle is the reduction of vortex-line energy, being their typical dimensions in the range of tens or few hundreds of nanometers. More recently, the advent of powerful nanofabrication techniques has allowed a further development and deployment of this concept. For example, uniaxial nanogroove structures have been used to demonstrate the transition from isotropic to anisotropic flux penetration regimes by tuning up the working temperature [16] and a DC-tunable microwave low-pass filter has been achieved by the construction of asymmetric nanogroove morphologies [7]. Taking a step further, here we put the focus on the extension of

* Corresponding author.
E-mail address: anabadia@unizar.es (A. Badía-Majós).
[1] Authors contributed equally.

https://doi.org/10.1016/j.apsusc.2024.161214
Received 3 July 2024; Received in revised form 2 September 2024; Accepted 9 September 2024
Available online 21 September 2024

the magnetic flux guiding process along quasi-2D channel architectures, i.e. on the fabrication of pathways enabling to manipulate the magnetic flux piercing the superconducting film, either by concentrating or diverting it from a specific area of the device. Superconducting Nb thin films have been selected for this study for its favorable properties (highest T_c of elemental superconducting materials, type II, widely used and grown worldwide) and technological relevance. It finds applications in planar resonators [11], particle accelerators [17], etc. for which relevant physical effects could be affected by surface nano-structuring. The application of surface tailoring technologies to materials with higher complexity (in particular to high temperature superconductors) is still a challenge to be addressed in future research.

Our proposal relies on a one-step processing approach that functionalizes the material by modulation of its surface topography in the submicron scale. Taking advantage of recent progress in laser technologies for material processing, one may induce corrugation of surfaces with control over: (i) the lateral periodicity, (ii) the depth, and (iii) the local orientation of the topographical grooves, all these with minimal alteration of the material itself. In fact, direct laser processing enables a versatile matter manipulation via irradiation with ultrashort (femtosecond) controllable laser pulses. Remarkably, owing to the intrinsic thermalization processes related to the interaction of matter and ultrafast laser pulses, one gets rid of unwanted heating effects [18]. Therefore, material structure preserving modifications, such as the good match between film and substrate are allowed. In particular, this processing method has been used to produce quasi-parallel surface patterns, the so-called Laser-Induced Periodic Surface Structures, LIPSS. Often termed simply “ripples”, LIPSS are a universal phenomenon that manifests during the laser processing of solids upon irradiation with coherent laser radiation [19–21]. Hitherto, it has been applied to different materials and for different functionalities as iridescence of surfaces, wetting control (hydrophobic-philic surfaces), medical cell growth or tribological uses. Details on these applications may be found in Refs. [22,23]. Phenomenologically, quasi-periodic arrangements of rippled lines or other surface features with spatial periods Λ of the order of the irradiation wavelength λ or even far below are formed in “self-ordered” ways after multiple-irradiation events in the focus of the pulsed laser beam. LIPSS arise from coherent optical scattering and (intra-pulse) interference effects at nanoscale surface defects along with subsequent positive (inter-pulse) feedback [22,24]. Even if the seeding of LIPSS always arises from electromagnetic effects, subsequent matter-reorganization (e.g. via thermal melting and hydrodynamic effects) may additionally affect the final surface topographies [21,25–29]. LIPSS being already present in the laser irradiated spot, can be "coherently linked" together [30] via laser beam scanning approaches for covering the desired macroscopic surface areas.

For the metal niobium, different types of LIPSS were reported in the literature. Most prominently so-called low spatial frequency LIPSS (LSFL) with periods $\lambda/2 \leq \Lambda \leq \lambda$ form in the direction perpendicular to the linear laser beam polarization for sub-ps laser irradiation [31–34]. It is generally accepted that the LSFL originate from coherent scattering and interference effects of the incident laser radiation at the microscopically rough surface, eventually leading to a spatially modulated absorption of the optical radiation. For suitable optical properties of the irradiated material, this may include the excitation of Surface Plasmon Polaritons (SPPs) [21]. Moreover, Pan et al. reported the formation of high spatial frequency LIPSS (HSFL) with 290 - 350 nm sub-wavelength spatial periods ($\Lambda \ll \lambda$) being parallel to the laser beam polarization, upon irradiation with near-infrared laser radiation ($\lambda = 800$ nm) using pulses with a duration of 100 fs [31].

Outstandingly, the pulsed-laser irradiation technique offers important advantages with respect to alternative methods such as heavy ion irradiation, nanolithography or chemical routes. In particular, it is eco-friendly, scalable and efficient, allowing to cover large surfaces within a short time, it has the possibility to tailor the pinning landscape at will and with high resolution. Furthermore, the presence of undesired chemical reactions, such as oxidation of the metal film, may be avoided by performing the process under a controlled inert atmosphere.

As a matter of fact, it is known that the morphological transformation of superconducting Nb induced by laser patterning gives way to conspicuous anisotropy in its electromagnetic response [32,35]. In the case of thin films, LIPSS induce a noticeable anisotropy factor $J_{c\parallel}/J_{c\perp}$ in the ratio of the critical superconducting current densities flowing either parallel ($J_\parallel$) or perpendicular ($J_\perp$) to their direction [35]. Thus, the electric current density $\boldsymbol{J}$ flows preferentially along the LIPSS ridges. In addition, recalling, that in type-II superconductors, flux penetration takes place in the form of incoming vortices (magnetic flux quantum units, i.e.: $\boldsymbol{\Phi}_0$) boosted by the Lorentz-like force and restrained by the pinning barriers, defined by the topographical undulations themselves, one straightforwardly finds that flux preferentially penetrates along the LIPSS.

In this article we explore the magnetic flux guiding capacity induced by imprinting conjoined domains of surface LIPSS with appropriate orientations so as to control locally the critical current density. We will always refer to LSFL-type LIPSS for which the laser processing parameters were optimized. Dedicated simulation studies based on the Nb optical response confirm this work hypothesis (see Sec. S1.1 of the Supplementary Material). Nanocrystalline Nb thin films deposited on a silicon wafer, with initial thickness of 200 nm were processed with an ultraviolet pulsed laser (343 nm wavelength, 238 fs pulse duration). The flux channeling effects and their physical origin in these 2D structures are studied by Magneto-Optical Imaging (MOI), together with data inversion techniques applied to the experimental profiles, and analyzed in terms of the Critical State model (CS model) [36,37] for the penetration of magnetic flux in type-II superconductors. Scanning and Transmission Electron Microscopy (SEM, TEM) as well as topographic and conductive Atomic Force Microscopy (AFM & cAFM) data are used in order to verify the surface topography, and to analyze the correspondence between topographical characteristics and magnetic flux profiles. Global superconducting properties of the laser processed films are characterized by SQUID magnetometry.

2. Materials and methods

2.1. Fabrication

2.1.1. Film deposition and sample shaping

Thin films of Nb with a thickness of 200 nm were deposited onto Si/SiO_2 wafers, using radio-frequency magnetron sputtering. The Nb physical vapor deposition was conducted at a rate of 0.1 nm/s under an Ar pressure of 5 Torr, after pumping down the chamber to a base pressure of $4 \cdot 10^{-8}$ Torr.

Before laser patterning, 4×4 mm^2 samples were laser-cut using a pulsed green laser (Light Conversion, Vilnius, Lithuania, model Carbide CB3-40 W, $\lambda = 515$ nm, $\tau_p = 249$ fs) working at a pulse repetition frequency $f_{rep} = 10$ kHz and a laser scanning speed of 5 mm/s. Subsequent to the cutting process, the samples were ultrasound cleaned in isopropanol for 15 min.

2.1.2. Laser patterning

For the surface nanopatterning of the thin film, the above described laser with a wavelength of $\lambda = 343$ nm was used, along with a pulse duration $\tau_p = 238$ fs. At the working distance, the output laser beam exhibited a spatially Gaussian energy profile with an elliptical spot, where $1/e^2$ beam diameters were $2a \times 2b = 36 \times 60$ μm^2. An optimization process was performed in order to determine the laser parameters for sample processing, resulting in pulse energies in the range 3.40–3.98 μJ, laser scan speed of 125 mm/s, pulse repetition frequency $f_{rep} = 20$ kHz, and distance between scan lines of 8 μm, for the different samples under study, and in a controlled Ar atmosphere (under gas flow in an open chamber). The inert atmosphere was used in order to minimize the effect of oxidation processes that lead to perceptible

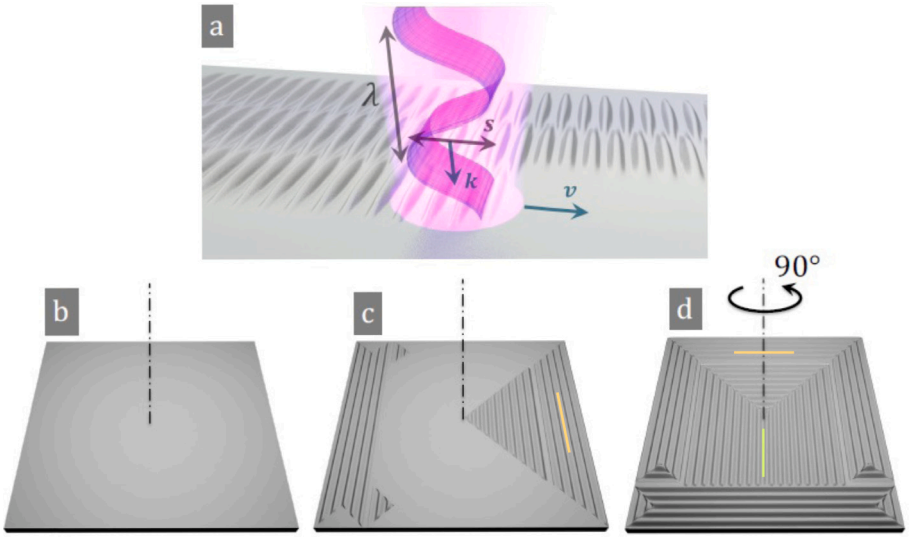

Fig. 1. Sketch of the laser irradiation process. (a) The laser beam scans over the film surface, with its linear polarization aligned with the scanning direction. The corrugation of the surface emerges perpendicular to this direction. As sketched in (b–d), complex domain structures were created from the pristine sample (b) by using a two-step process according to pre-established configurations. This particular example corresponds to the sample that will be named after *top-hat*. Firstly, some selected areas were irradiated to generate LIPSS parallel to the orange segment (c). Secondly, the sample was rotated 90° and then (other) selected areas were irradiated to create LIPSS in the orthogonal direction, i.e. parallel to the green segment (d). Plain gray corresponds to non-irradiated areas while stripped areas are indicative of the laser-scanned parts.

reductions of the critical temperature T_c [35], not to mention the contribution to remove possible debris particles through the gas flow. The laser scan speed and the distance between scan lines were carefully selected for the above levels of pulse energies for obtaining a nearly uniform nanostructure distribution in the Nb thin film scanned area. A basic sketch of the laser-patterning process is included in Fig. 1. We notice that, in all cases, the beam scanning direction was parallel to the polarization of the beam. This relative orientation is not critical for the generation of LIPSS, although it may have effects on the overall morphology (specifically on their length) according to previous studies in other materials [38]. Then, in order to avoid data dispersion we were careful to keep the angle constant throughout the treatments.

In order to create the various patterns considered, subsequent to the calibration process, spatially resolved laser treatments were performed. Subsequently, the sample was rotated precisely by 90° using a goniometer and a home-made setup. Laser treatments were then conducted on the non-treated areas to produce LIPSS perpendicular to those generated previously, achieving the desired pattern. Finally, in order to obtain a centered pattern, as well as to avoid boundary effects due to imperfections in the cutting process, an additional laser treatment was applied aiming at the removal of Nb in excess, with inner dimensions 3×3 mm^2 by applying an average power of 1.35 W to the original 4×4 mm^2 platelet in a two-fold process. In brief, we end up with a perfect square-shaped film area with aligned LIPSS morphology, surrounded by a small inert frame of uncoated substrate.

2.2. Microstructural characterization

2.2.1. SEM and TEM analysis

Surface characterization was carried out using a MERLIN field-emission scanning electron microscope (FE-SEM) (Carl Zeiss in Jena, Germany), equipped with an energy dispersive X-ray spectroscopy (EDS) system from Oxford Instruments (Abingdon, UK). The FE-SEM was operated at 5 kV and utilized secondary electron (SE), in-lens, and energy-selective backscattered (ESB) detectors. Cross-sectional TEM images were taken with a Tecnai F30 microscope of FEI (Lincoln, NE, USA). With this aim, several lamellas were prepared using a Focused Ion Beam (FIB) in a Dual Beam Helios 650 apparatus of FEI. Prior to the FIB-lamella extraction, samples were coated with C-Pt protective layers.

2.2.2. Atomic force microscopy (AFM and cAFM)

Atomic force microscopy measurements were performed with a scanning probe microscope (SPM) Ntegra Aura system of NT-MDT at room temperature in order to analyze the LIPSS topography. Quantitative local electrical resistance measurements were also performed at room temperature using the c-AFM mode of a CSI Instruments Nano-Observer AFM. The analysis of the AFM measurements as well as the 2D-Fast Fourier transforms from SEM images were carried out using Gwyddion software.

2.3. Magneto-optical imaging

Magnetic flux penetration analysis along the laser-patterned areas was performed using the magneto-optical imaging technique. The employed experimental configuration mimics a commercial polarization microscope. A light beam emitted by a LED lamp passed through a green filter (550 nm) and a linear polarizer before reaching a Faraday active indicator. The indicator in this study consisted of a 3.5 μm-thick layer of Bi:YIG, epitaxially grown on a 450 μm-thick $Gd_3Ga_5O_{12}$ (GGG) transparent substrate, with a 100 nm-thick Al mirror deposited on the optically active layer to ensure adequate reflection of the incident light. The linearly polarized light traversed the GGG substrate and the Bi:YIG layer within the indicator, undergoing a polarization direction rotation corresponding to the local magnetic field. Subsequently, the light was reflected by the mirror, retraced its path through the indicator and the objective, and finally reached an analyzer. The collected light was then directed to a high-resolution CCD camera situated atop the microscope unit, producing an image in which the intensity contrast directly represented the magnetic field distribution. More technical details may be found in Ref. [39].

2.4. Magnetic characterization

The complex AC susceptibility, $\chi_{ac}(T)$, with in-phase χ' and out-of-phase χ'' components, was measured at zero DC magnetic field and AC drive magnetic field (sine wave of amplitude $\mu_0 h_0 = 10$ μT, and frequency $f = 10$ Hz) in a SQUID magnetometer (MPMS-5T from Quantum Design, San Diego, CA, USA), in order to determine the superconducting critical temperature, T_c of the samples, using the onset of diamagnetism criterion. In pristine films we found $T_c = 8.9$ K,

while laser treated samples show a reduced value $T_c = 8.7$ K (full curves contained in the Supplementary Material section).

All magnetic measurements were performed on the above described square samples with the magnetic field applied perpendicular to the surface and after zero field cooling. For each measurement, a reset of the superconducting magnet was performed previous to sample cool down in order to eliminate the remnant magnetic field.

3. Calculations: computational methods

3.1. Critical state modeling

Magnetic flux penetration in the laser patterned Nb samples has been simulated by a numerical extension of the CS model in type-II superconductors. In its original form [36,37], the model postulates the *criticality* condition $J(x) = 0, \pm J_c$ for the circulating current density within the superconductor in 1D geometry (slabs and long cylinders). In its simplest form J_c, the so-called critical current density, is a material dependent parameter. Then, the actual magnetic field profile is established by integrating Ampères's law, implementing boundary conditions on the sample's surface and implicitly applying Faraday's law for choosing the +, − or 0 option. As a result, one obtains the actual flux penetration profile for an arbitrary route of the excitation field. In brief, this model is physically meaningful for type-II superconductors with strong flux pinning mechanisms. Then, the magnetic flux profile is basically determined by postulating the maximum gradient law ($J(x) = 0, \pm J_c$). This scenario is valid as long as the sample is well penetrated by ''anchored'' flux tubes and thermal agitation negligible. In our experimental conditions (low temperatures and fields in the range of mT) both conditions are satisfied. In fact, for the case of flat samples, flux penetration occurs for fields well below H_{c_1}, i.e.: $H_{\text{ENTRY}} \approx H_{c_1}\sqrt{0.36\zeta}$ [40], with ζ the platelet aspect ratio ($\simeq 7\times10^{-5}$ in our samples). On the other hand, the CS model will be used in upgraded form (2D model geometry for thin films in perpendicular field [41]), which is also justified by the small value of ζ. In this situation, not only the sign, but the local orientation of the current density is unknown in each point. In the quasi-steady regime, the electromagnetic problem is solved by taking benefit of the divergenceless property of the current density together with the negligible sample thickness d. These conditions allow us to pose the problem in terms of a scalar function, the so-called *streamfunction* $\sigma(x, y)$ that relates to the surface current density (averaged over thickness) by $\boldsymbol{K} = -\hat{z}\times\boldsymbol{\nabla}\sigma$ [42] being

$$\boldsymbol{K}(x,y) = \int_{-d/2}^{d/2} \boldsymbol{J}(x,y)\,dz\,. \tag{1}$$

Finally, the application of Faraday's law together with the superconducting material law is accomplished by an optimization problem [41,43]. One has to minimize the functional

$$\mathcal{F}[\sigma_{n+1}] \equiv \frac{1}{2}\int\!\!\int_{\Omega}\left[\frac{\boldsymbol{\nabla}\sigma_{n+1}(\mathbf{r})\cdot\boldsymbol{\nabla}\sigma_{n+1}(\mathbf{r}')}{\|\mathbf{r}-\mathbf{r}'\|} - 2\frac{\boldsymbol{\nabla}\sigma_{n}(\mathbf{r})\cdot\boldsymbol{\nabla}\sigma_{n+1}(\mathbf{r}')}{\|\mathbf{r}-\mathbf{r}'\|}\right]d\mathbf{r}\,d\mathbf{r}' + 4\pi\left(H_z^{a,n+1} - H_z^{a,n}\right)\int_{\Omega}\sigma_{n+1}(\mathbf{r})\,d\mathbf{r} \tag{2}$$

with Ω the surface of the film, $H_z^{a,n}$ the $z-$component of the applied external field, and the subindices n and $n+1$ used to indicate two successive time layers. The superconducting material law (action of barriers for the flux dynamics that are codified by the critical value $K_c = J_c d$) enters through a restriction function that accompanies the minimization process and models the anisotropic and local character of the current density. In our case, related to the preferential flux slippage along given directions, it takes the form

$$\frac{K_{\parallel}^2}{\Gamma^2} + K_{\perp}^2 \le K_c^2\,, \tag{3}$$

with $K_{\parallel}, K_{\perp}$ the current density components either parallel or perpendicular to the "easy direction" defined by the LIPSS at a given point. Minimization is performed step by step, adapting the response of the sample to the external excitation process. Anisotropy and inhomogeneity are introduced through the local parameter values $\Gamma(x,y) \equiv K_{c\parallel}/K_{c\perp}$ as sketched in Fig. 3. Further details concerning the background and numerical implementation of the model (MATLAB encoded) may be found in [35]. In particular, as explained in that reference, the critical current parameter of Nb is better described as a function of the local field, i.e.: $K_c = K_{c_0}[1 + B/B_0]^{-2}$. In this work, this property acquires relevance because flux is purposely concentrated in particular spots. In fact, such dependence produces more realistic predictions of the measured electromagnetic quantities.

3.2. MOI inversion procedure

The inversion of the MO images was performed following the technique developed in Ref. [44]. The indicator thickness and distance between the sample and the indicator, which are key components to compute the inversion kernel, were set to 3 μm and 10 μm, respectively. As the superconducting sample covers most of the imaging area, we numerically extended the images by padding them with the value of the applied field so that the total image size is three times the original one. This leaves a region 3 mm wide where $B_z = \mu_0 H_a$ all around the sample. This was done to discourage the inverted current lines from flowing through the periodic boundaries created by the Fourier-based technique, thus ensuring the current lines form closed loops.

4. Results

4.1. Tailoring Nb thin films: laser-processed metasurfaces

Taking advantage of the observed anisotropy of the critical current density $\boldsymbol{J}_c$ for these laser-patterned samples [35], we designed and fabricated proof-of-concept structures aimed at controlling the magnetic flux penetration in the superconducting state (Fig. 2). In this figure, we sketch the line-wise meandering laser scanning protocol and the analyzed laser-patterned designs. The targeted orientation of the LIPSS domains is obtained by commanding the laser beam polarization direction (Fig. 1). As shown in Fig. 2a–c, basically parallel groove nanostructures are achieved which, on average, display a lateral spatial periodicity of ≈ 260–270 nm, and a depth (from crest to trough) of $\approx 80 \pm 15$, nm. Figs. S1 and S2 of the Supplementary Information provide further details on the experimental results, as well as on the theoretical simulation of the emerging LIPSS spatial frequencies structure as deduced from the optical properties of Nb.

Conceptually [35], by using LIPSS, one might divert the natural tendency of the magnetic flux penetration, otherwise strongly influenced by demagnetizing effects in 2D geometry. The tested featured designs are (by order of complexity): (i) the *fringe structure* in Fig. 2d, aimed at the channeling of magnetic flux along the central line of pristine Nb, (ii) the *cross geometry* (Fig. 2e) aimed at "compensating" the preferential penetration of magnetic flux along the center of the film sides, and (iii) the *top-hat geometry* (Fig. 2f), a specific pathway for the penetration of magnetic flux, constructed by defining a structure of magnetic domains on the film surface. This design aims to "guide" the penetration of flux along a tailored path, which is flanked by parallel ridges of the LIPSS in the neighboring laser-patterned domains (expectedly confining the flux dynamics within the path by hindering the penetration perpendicular to the LIPSS). For brevity, Fig. 2 shows specific instances for each geometry, though equivalent designs with different sizes were also tested.

4.2. Routing magnetic flux penetration

4.2.1. Magnetic flux channeling and diversion

In Fig. 3, we present direct imaging of the magnetic field landscape obtained by the MOI technique, demonstrating the diversion of flux

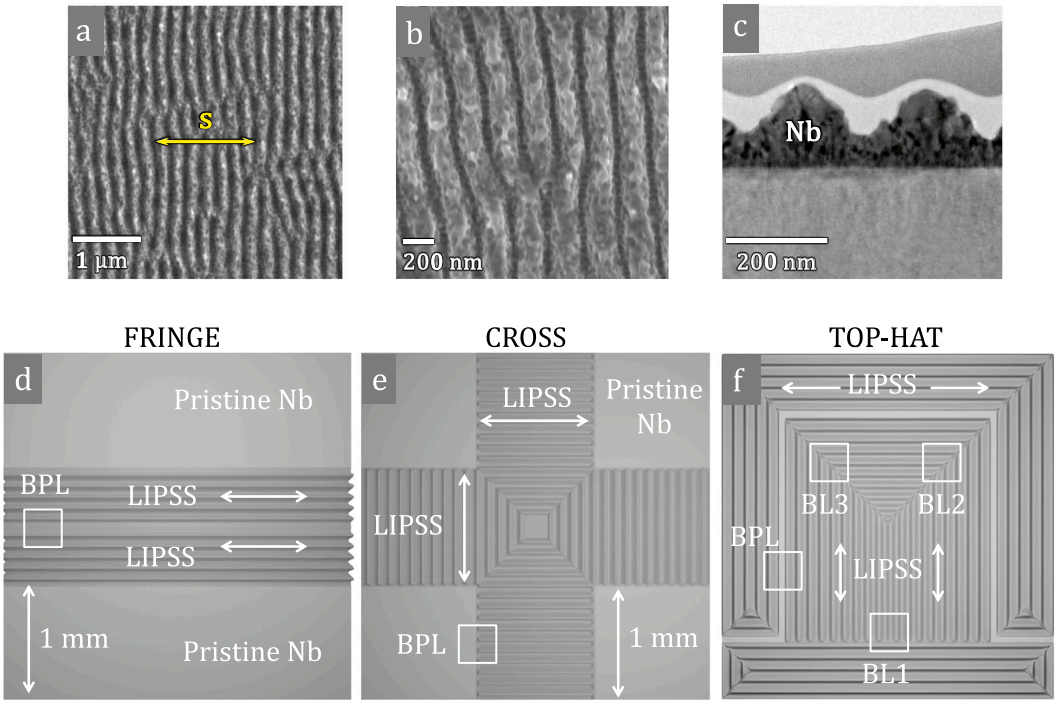

Fig. 2. Panels (a–b) show top-view SEM images of a LIPSS domain observed by secondary electrons and in-lens detector, respectively, and (c) a cross-sectional TEM image. The yellow double arrow indicates the laser polarization. (d–f) show the geometries investigated in this work. The domain structures in (e) and (f) were created by programming the beam trajectories and rotating the sample by an angle of 90°, according to the pre-established configurations as explained in Fig. 1. In the three panels, plain gray corresponds to non-irradiated areas while stripped areas are indicative of the laser-scanned parts. The transition between pristine and irradiated zones, as well as the boundaries separating the areas with different orientation of the LIPSS are indicated. Small rectangles point out boundary regions that were investigated in detail (as shown in Section 5): BPL is for Boundary between Pristine & LIPSS regions and BL for Boundary between LIPSS domains.

penetration induced by texturing the sample with domains of properly oriented LIPSS. Images correspond to two values of increasing out-of-plane applied magnetic fields after zero field cooling (ZFC) at a stable temperature of $T = 8$ K for the fringe and cross-shape geometries. According to SQUID magnetization measurements (see Sec. S2.1 of the Supplementary Material), this temperature selection guarantees the restraint of unstable flux avalanching processes [45], which are a prominent effect well below T_c.

We notice that the *fringe* geometry displays a noticeably enhanced flux penetration along the central channel (Fig. 3a,b), even beyond the distance reached in the pristine region. In fact, as shown in Fig. 3b, the LIPSS act as a barrier for the penetration of magnetic flux. On the other hand, the transversal LIPSS structure in the *cross-shaped* geometry "protects" the central part of the sides from the usual enhanced flux penetration across that spot (Fig. 3c,d). These features have been repetitively observed in a wide range of temperatures, as displayed in the Supplementary Information (Sec. S2.2). In order to understand the physical origin of the experimental behavior observed in MOI, we carried out simulations of the penetration of magnetic flux. To that end, we put forward theoretically predicted current density streamlines and related magnetic flux profiles that capture the principal features revealed in the experiments (Fig. 3,i-l). In brief, numerical simulations have been performed by a CS formulation [36,37], that takes into consideration a non-homogeneous pinning landscape (as described in Section 3.1 in the Methods part). This coarse grained electromagnetic model uses a conduction law whose main parameter is the so-called local critical current density J_c (maximum non-dissipative current density allowed by the material at a given sample location). In terms of J_c, the laser treated areas are simulated by using an anisotropy factor Γ, as in Eq. (3), i.e.: the ratio between the critical current density flowing parallel ($J_{c\parallel}$) and perpendicular ($J_{c\perp}$) to the LIPSS, and relative to the pristine Nb value. As sketched in the plot and justified below, here we have used: $\Gamma = 3$, i.e.: $J_{c\parallel} = 3J_{c\perp} = 3J_c$, with J_c the original value of the isotropic critical current density, characterizing the untreated Nb film regions.

We note that our results indicate that the critical current density is increased along the LIPSS (i.e.: parallel to the LIPSS ridges), and keeps its original value perpendicular to them. We also point out that the ratio $\Gamma = 3$, that produces good agreement with the MOI observations was obtained from the experimental discontinuity-line criterion applied to our MOI experiments in saturated conditions (the details of this analysis may be found in the Supporting Information, Sec. S2.2).

Finally, it must be underlined that, in order to reproduce the experimental observations, a reduction of the critical current density within the boundary regions between patterned/unpatterned regions has to be assumed (see Fig. 3e–h). In simple terms, the enhanced flux penetration along the boundaries between the pristine and laser treated areas is concomitant with the sag in the current density streamlines. Such effect denotes a decrease in the modulus of the circulating current density J because, in steady state conditions, the separation between the streamlines is inversely proportional to J.

Notoriously, the phenomenological CS model (in particular, its simplified numerical template) captures the main features of the experiment, i.e.:

(i) Magnetic flux penetration (darker areas indicate higher flux density) is preferential along the boundaries in between patterned and unpatterned regions.
(ii) In the *fringe* structure, flux penetrates faster along the central channel, followed by the penetration along the lateral boundaries and the non-treated zones, and, eventually, along the central part of the treated areas.
(iii) In the *cross* structure, the flux density on top of the untreated square regions (corners of the sample) develops a deformed pyramidal roof structure, with edges deviated from the diagonal of the square.

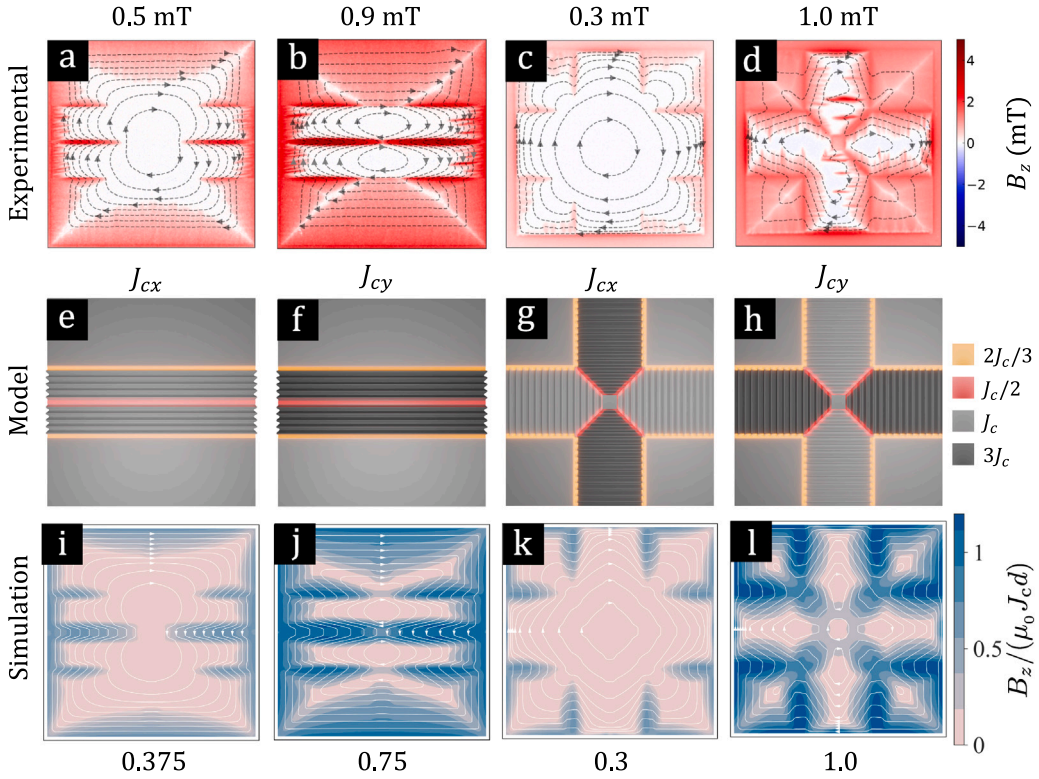

Fig. 3. Magnetic flux penetration and current density streamlines in a laser patterned Nb film with the tailored *fringe* and *cross-shaped* structures of LIPSS parallel to the sample's perimeter. The experimental MOI images (a–d) were obtained at the temperature $T = 8$ K and for the out-of-plane applied fields $\mu_0 H_a$ (mT) indicated on top. The reconstruction of the current density streamlines based on the inversion of the recorded magnetic flux density on top of the sample B_z is also shown. Arrowheads indicate the flow direction of the streamlines. The intermediate panels (e–h) sketch out the anisotropic and inhomogeneous current density model used in the simulations below. The lower panels (i–l) show theoretically predicted current density streamlines induced in the film obtained from the critical state model (see text), together with the related density plots of $B_z(x, y)$. Normalized dimensionless units are used both for the applied field and the resulting flux density (J_c is the critical current density and d is the thickness of the sample).

(iv) Eventually, at higher magnetic fields, the magnetic flux reaches the central area of the cross, by entering along the diagonal boundaries between the domains.
(v) The flux density profiles within the patterned domains of the *cross* develop a fish-like silhouette (Fig. 3d,l) that reveals the underlying anisotropy, i.e.: $B_z(x, y)$ penetrates faster parallel to the LIPSS.

Additional experimental evidence of the above features are available in the Supplementary Information (Figs. S8 and S9).

Summing up this section, flux dynamics has been tailored by the underlying pattern of isotropic/anisotropic LIPSS-covered areas and their boundaries. Specifically, the natural trend in square platelets in transverse field, i.e.: the inhomogeneous penetration of magnetic flux, mostly across the central part of each side [42], has been modified. In the laser treated samples, flux is driven along the interfaces of the areas patterned with LIPSS, that operate as principal flux distributors, eventually followed by channeling along the LIPSS themselves when flux enters the laser treated areas.

4.2.2. Steering magnetic flux: fabrication of pathways

Taking advantage of the above observations, we designed a surface topography that combines neighboring laser treated and untreated domains, acting as a magnetic hose for the flux penetrating in the film, i.e.: the top-hat structure sketched in Fig. 2f. Recall that the targeted "magnetic path" combines the enhanced penetration along the boundary lines and the hindered drift of flux across the flanking ridges defined by the LIPSS.

We first concentrate on the laser-patterned surface domains. A close inspection by SEM of the boundary regions indicated in Fig. 2f is presented in Fig. 4. The microstructural detail around the channel (Fig. 4a, region BPL) reveals a ≈ 30 μm-wide band of, allegedly, original Nb surrounded by a transition zone, that eventually connects to the nanostructured area (the targeted gap between the centers of the laser beam at the channel sides was 50 μm). The transition band (10 μm-wide) displays an induced nanoscale roughness but no pronounced LIPSS, which in fact, start progressively forming beyond this point and are aligned parallel to the channel. Here, it is important to recall that in this case the laser beam scanned the sample perpendicular to the channel, in a meandering bidirectional trajectory. Therefore, the transition boundary is formed by the superposition between the successive beginning/end points of the scan lines, and may be affected by power delivery and beam acceleration issues related to the smaller overlap of the laser spot energy density profiles.

The morphological characteristics of the transition are similar to those BPLs in the cross sample shown in Fig. S3 of the Supplementary Material, but wider in that case. The difference stems from the fact that, owing to the targeted arrangement of the LIPSS, for the latter case, the laser scan was parallel to the boundaries and the overlap was smaller owing to the elliptic shape of the spot (see Methods). However, in both cases, the widths of the transition zones are of the same order and always smaller than the semi-axes of the elliptic Gaussian laser beam.

In fact, as described in Ref. [35], the formation of well-structured LIPSS is a two-fold process strongly dependent on the initial profile of energy density deposited by the laser beam and on its superposition with the successive pulses in the scanning process. Consequently, a well defined boundary requires a precise overlapping strategy compromising the finite beam overlap and the precise allocation of the sample's rotation axis for the case of complex LIPSS-patterned domain geometries. With our setup, a mismatch of about than 10–15 μm was achieved and better and better results obtained by a "trial and error"

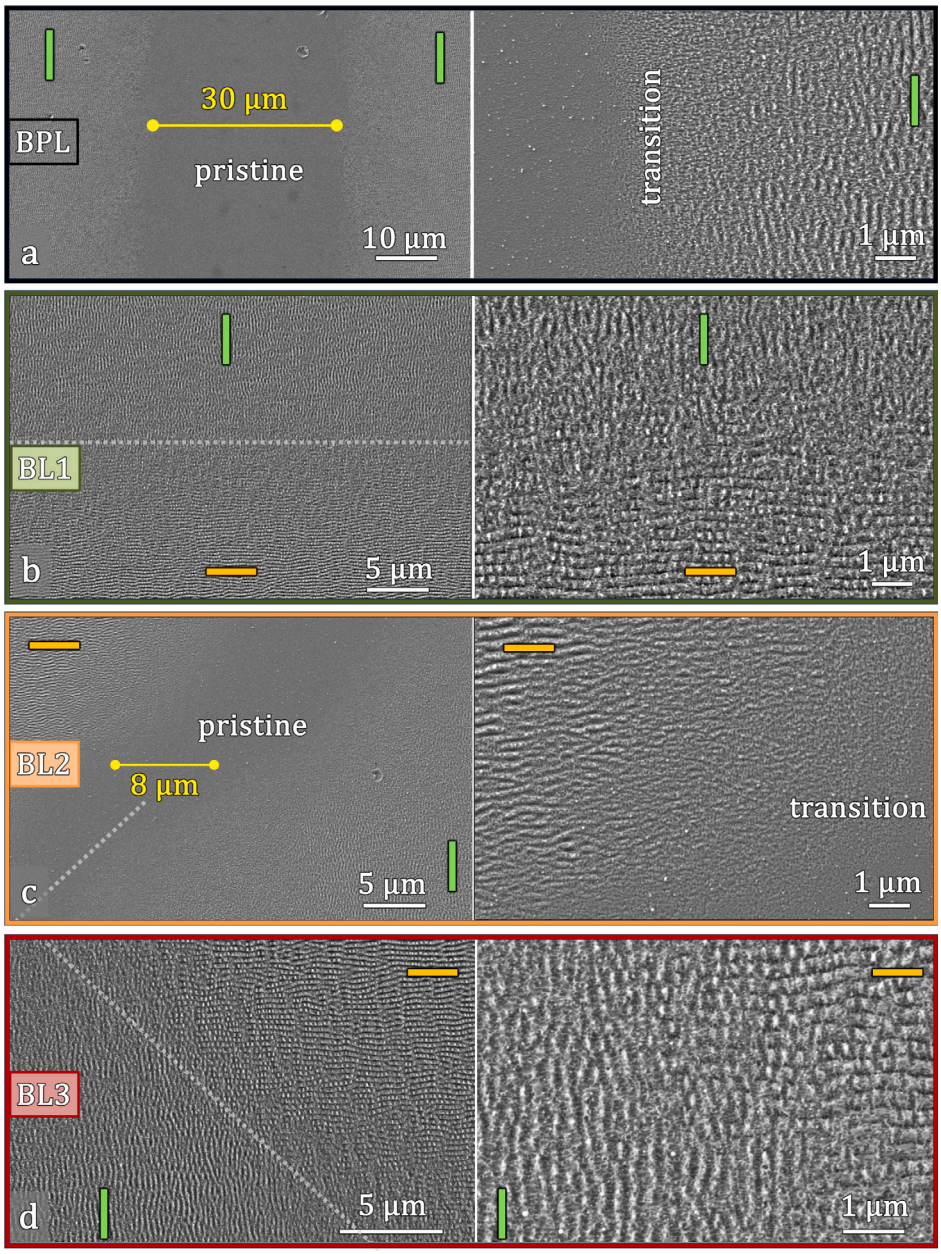

Fig. 4. SEM images of the boundary area BLP (a), BL1 (b), BL2 (c), BL3 (d) marked in Fig. 2 for the top-hat geometry. For each case, different areas with different magnifications are displayed. Dotted white lines are a guide to the eye for better visualization of the laser-patterned domain boundaries. The colored bars indicate the microscopic orientation of the LIPSS (orange: horizontal, green: vertical).

strategy positioning the sample on the holder, limited by the positioning and repeat accuracy of the motorized stages. More advanced laser-scanner technology with full ("single-spot" (pixel)) control of polarization direction, scanning direction and scan velocity is envisaged for the future.

The transitions of the surface topography in between domains with different LIPSS orientations (spots BL1, BL2 and BL3) are detailed in Fig. 4b–d. In the regions identified as BL1 and BL3, LIPSS of the neighboring domains intersect around the orientational boundary dividing them as suggested by the highlighted discontinuous lines in the images. On the contrary, in the zone BL2 there is a gap between them, with a transition band similar to the one shown in Fig. 4a. By comparing SEM and MOI images of this sample, the influence of the different morphological characteristics of the intersections between LIPSS domains on their superconducting behavior will be analyzed.

Fig. 5 shows a selected set of MOI images obtained for the top-hat path upon increasing applied magnetic field from 0 to 1.2 mT after ZFC down to 8.28 K.

Initially, flux enters the sample following the designed path, symmetrically from both sides. In fact, by closer inspection of the MOI images around the path (see inset in Fig. 5 at 0.3 mT), it is noteworthy that the field is higher at the very boundaries than at the central part. Then, at applied fields of 0.3–0.4 mT the magnetic flux pattern deforms properly, following the drawn path. However, against expectations, upon further increasing the field, some flux leaks in at the separation between some neighboring domains and eventually leaks along the LIPSS. Leakage takes place:

(i) partly along the initial penetration direction, thus following the boundary line (BL1) that separates two LIPSS's domains (aligned vertically/horizontally in its upper/lower side).

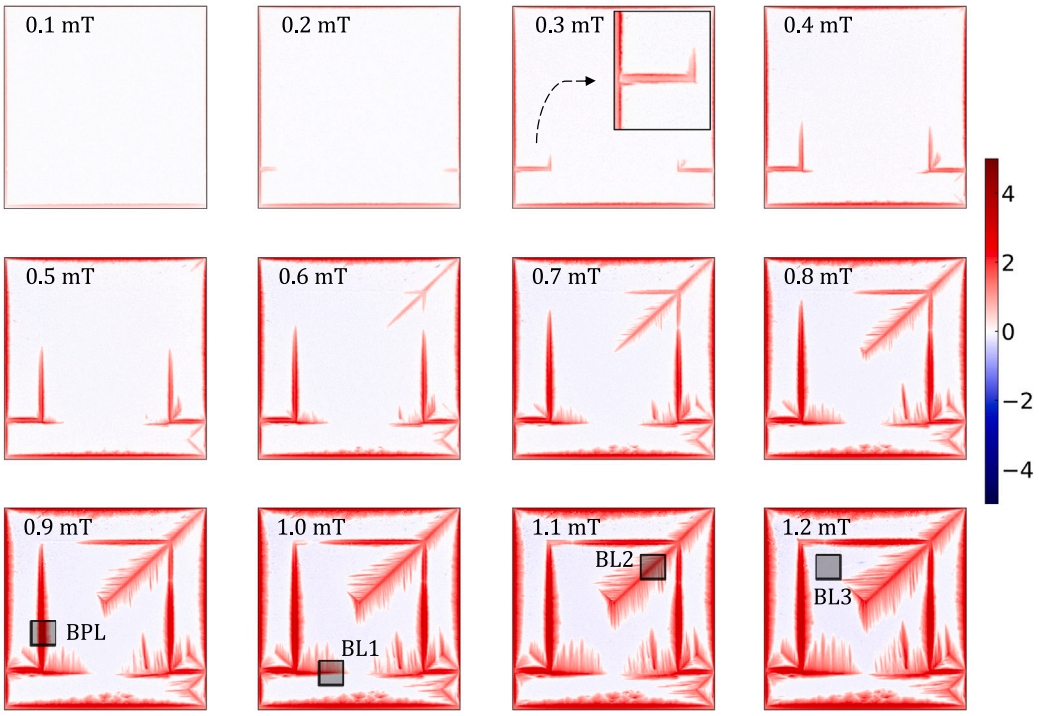

Fig. 5. Magneto-optical images of the flux penetration process in the top-hat channel described in Fig. 2f. The increasing values of the applied magnetic field are indicated on the successive steps. The thin film was zero-field-cooled to the base temperature of 8.28 K and field subsequently ramped up. Darker areas correspond to the higher values of the local magnetic field (basically along the top-hat channel), and are accompanied by ramifications along the neighboring LIPSS in the boundaries between orientation domains (compare to Fig. 2f). BPL, BL1–BL3 outline areas around the boundaries between domains, with the presence of LIPSS with different orientations that have been investigated in detail.

(ii) for fields higher than 0.6 mT, flux also enters along the upper-right large diagonal (BL2), again defined by boundary-lines between orientational domains. (Fig. 2).

Notwithstanding the above, the symmetrically disposed upper-left diagonal (BL3) shows a perfect behavior, that is, the induced supercurrents in this area of the sample allow appropriate shielding of the magnetic field, avoiding leaks from the designed flux channel.

From the above, one may conclude that well defined boundaries are necessary in order to achieve optimum channeling conditions (as revealed by comparison of the BL2 and BL3 zones), together with some further considerations as deduced from the non-perfect behavior in BL1. In Section 5, the flux penetration properties observed by MOI and described phenomenologically by the CS theory will be further connected to the laser induced microstructural properties through complementary experimental information.

4.2.3. *Parceling magnetic flux*

To this point, we have described the behavior of laser patterned metastructures under monotonic increasing field processes for the geometries sketched in Fig. 2. Below, we reveal a new feature emerging under alternating field cycles. More specifically, we show that by applying low frequency, i.e.: $\lesssim 100$ mHz AC cycles with decreasing field amplitude, one may fabricate and store flux packets of controllable size, consisting of alternating units of positive and negative flux (see Fig. 6).

As shown in the upper panels, by virtue of a few number of cycles, we achieve a rather robust structure of alternate positive/negative flux segments within the channel, of size Δ controllable by the rate of decrease of the applied field amplitude δH_a. We notice that the formation of these chains is rather independent of the actual environment surrounding the flanking LIPSS domains.

Again, from the physical point of view, the construction of these regular alternating flux density profiles also finds an explanation in the CS theory [36,37]. As shown in Fig. 6g,h, even the simplest formulation (Bean's model for infinite slabs in parallel magnetic field) predicts a "saw-tooth" profile of positive and negative flux bits when the applied field is cycled along the process $H_1 \rightarrow H_2 \rightarrow H_3 \rightarrow H_4 \rightarrow H_5$. For the more realistic 2D geometry accomplished in our experiments with thin films, the structure within the channels flanked by LIPSS domains is provided with high fidelity by the numerical solution of the CS model as displayed in the panel i of Fig. 6.

5. Discussion

The results presented so far provide evidence of the successful achievement of magnetic flux diversion and channeling on superconducting Nb thin films by an appropriate laser surface nanostructuring, in particular, as concerns the role of orientation domain boundaries. As shown in Section 4.2, the actual induced microstructural modifications induced by the laser at the inter-domain frontiers are crucial for the eventual behavior of magnetic flux. In particular, flux enters preferentially along the rough transition regions between pristine Nb and the domains of well-ordered LIPSS (BPL in Fig. 2f), and may be conveniently expelled from those areas with neat transitions between different orientations of the LIPSS (BL3 in Fig. 2f). This second condition is nevertheless not sufficient as one may notice by the flux leakage along the boundary BL1 in Fig. 5. As a thumbrule, the "clean transition" requirement must be adjoined with a second basic condition: within the flux free areas, shielding current loops should be allowed to flow with ease along shape-preserving paths following the configuration of the channel. This basic property of every flux screening distribution may be assessed from the observation of the current density loops in Fig. 3, together with the improvement of the behavior in the region BL1 by defining an oblique boundary, as it is noticeable comparing Fig. 5 and Fig. 6e.

In order to further investigate the properties of the above mentioned "rough" transition zones that restrain the flux penetration channels, additional experiments collected in Fig. 7, were performed. Fig. 7a,b shows the MOI intensity decay with temperature measured in different

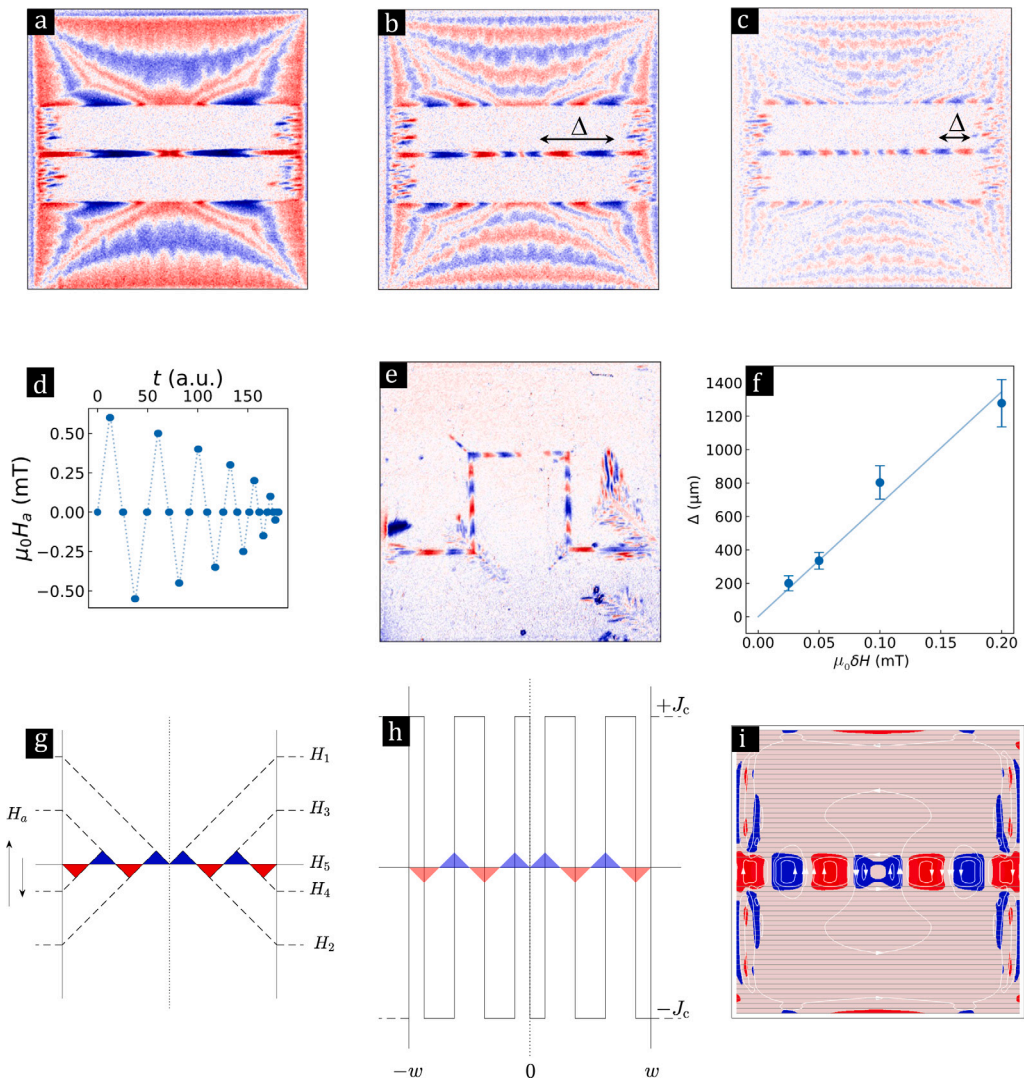

Fig. 6. Magneto-optical images of the *flux parceling* process along the channel of the *fringe* geometry (a–c) for different snapshots corresponding to the "magnetization" protocol shown in panel (d). (e): the same for the *top-hat* geometry. In the sequence (a–c), we used $T/T_c = 0.776$, and reductions of amplitude $\mu_0 \delta H_a = 0.2, 0.1, 0.05$ mT respectively, whereas panel (e) corresponds to $T/T_c = 0.91$, and $\mu_0 \delta H_a = 0.05$ mT. The same color bar as in Fig. 5 was used. In panel (f) we plot the experimental "flux packet" size Δ as a function of $\mu_0 \delta H_a$. Panels (g)–(i) depict the supporting theoretical framework. (g), (h) display the flux penetration and current density profiles induced by a demagnetizing process under Bean's model 1D approximation, while (i) shows the expected flux density and current density streamlines obtained through a numerical 2D model for a straight channel structure.

zones of the fringe sample after field cooling to the base temperature under an applied field of $\mu_0 H_a = 4$ mT and subsequently turning the field off. This allows an estimation of the local critical temperature, defined as the temperature where MOI relative intensity reaches the constant value beyond the transition. As compared to the value of the non-irradiated zones in the same sample, $T_{c,pristine}$, we observe a small decrease in the LIPSS-patterned regions, $T_{c,\mathrm{LIPSS}}/T_{c,pristine} \approx 0.975$, which further reduces to $T_{c,\mathrm{transition}}/T_{c,pristine} \approx 0.95$, in all BPL boundaries. On the other hand, cAFM measurements at room temperature across the magnetic flux channel of the same sample (Fig. 7c) indicate significant changes on the measured contact resistance by tapping against the region around the path.

The significant variations of the local electrical conductivity enable us to use the cAFM technique for mapping the different zones of the analyzed samples with excellent correspondence to the magnetic flux channels observed at low temperatures.

The topographical analysis around the *magnetic flux channels* (see Fig. 7d) reflects a progressive increase in surface roughness from the channel in agreement with SEM images. It must be mentioned that patterning occurs gradually, with an undefined spatial period in the transition area until, eventually, self-organization initiates and gives rise to the LIPSS. Note that the ripples near the boundary have significantly lower depths than those inside the LIPSS-patterned regions. Remarkably, the topographical changes observed by AFM around the magnetic channel are an indication of underlying changes related to the observed reduction of T_c and implied decrease of J_c observed by MOI. Whether these surface properties are the only factor affecting superconductivity at the local level deserves of further investigation. For this purpose, the observation of cross-sectional views of the full Nb layer at the regions of interest was addressed. Reference lamellas were prepared from the transition zone in the *cross-shaped* sample for TEM observation.

TEM images of the different zones are shown in Fig. 7e–g. In all cases, we observed a perfect pairing between the Nb film and the substrate, as well as the absence of cracks, thus ruling out detachments or mismatch as the origin of the depleted superconducting properties. We notice that the pristine area shows that the Nb layer is composed by very small grains (size about 20–30 nm) which are basically disposed in a columnar arrangement. In the transition zone (Fig. 7f), there are small protrusions at the surface (in consonance with SEM and AFM observations) and the film thickness decreases slightly (by 5–10%). The TEM images of this area show that the influence of laser is not restricted

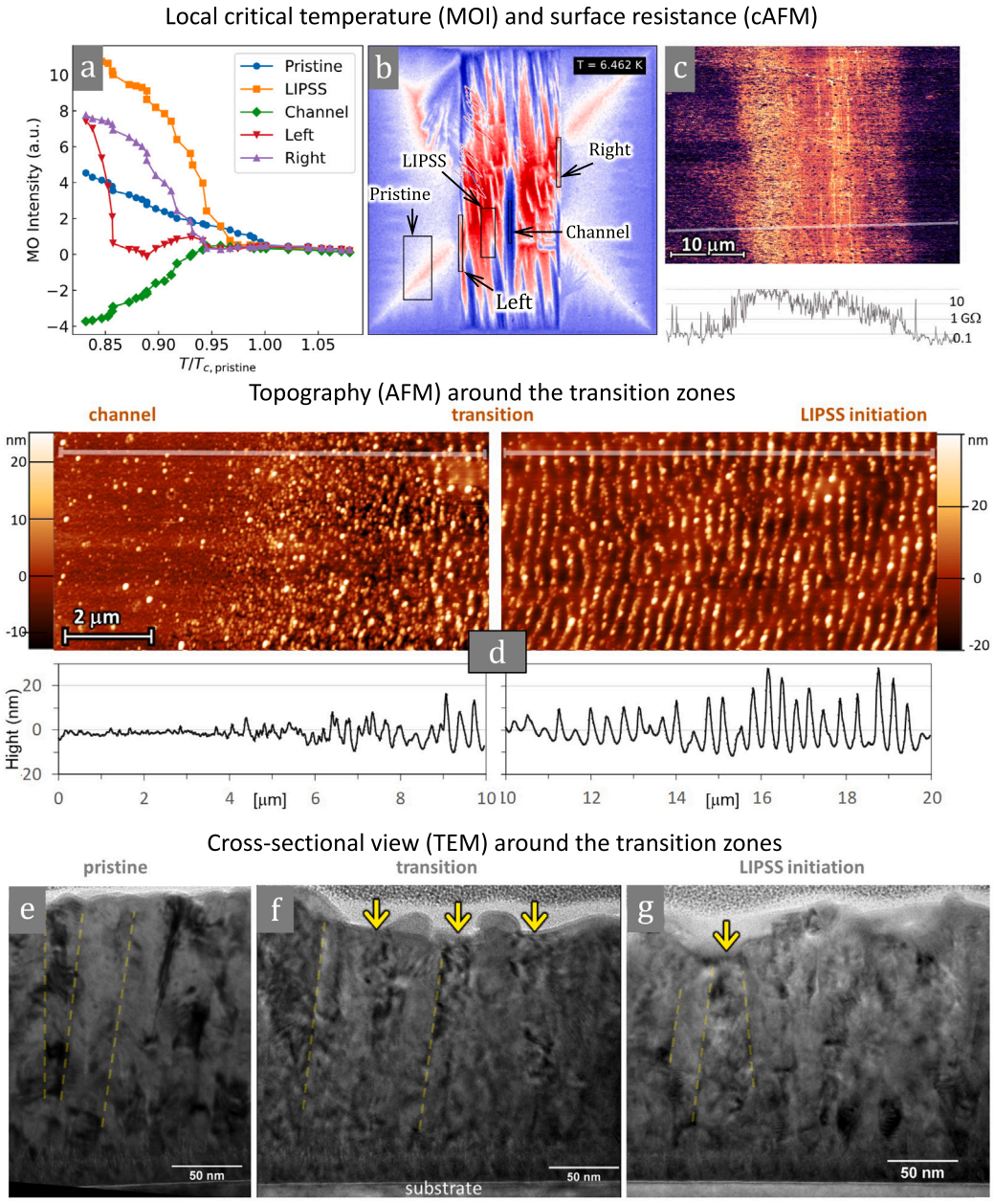

Fig. 7. (a) MOI intensity decay as a function of temperature at different zones (highlighted by squares in panel (b)), (c) cAFM image at room temperature around the magnetic flux channel of the fringe sample. The graph shows the resistance measured along the line drawn in the image above, (d) AFM images and corresponding line profiles near the flux channel of the top-hat sample (consecutive scans over 10×3.5 µm^2 areas). TEM images (cross-sections) of a non-patterned area (e) and BPL zone (f)–(g) of the cross sample. Dotted lines are a guide to the eye. Yellow arrows point to some grains featuring larger number of dislocations and defects.

to the surface or to a very thin layer below it. On the contrary, they reflect an increase in the number of dislocations and defects (larger number of darker lines in the images), specially in those grains pointed out by yellow arrows in the figure, in between the small surface protrusions. The columnar disposition of grains is still clearly visible. In the transition region close to the LIPSS (Fig. 7g) the disorder and number of defects further increases and the grain columnar arrangement becomes less clear. Note also that there is a small zone of ≈ 25 nm in depth, close to the Si-substrate, where the grains are smaller. This zone remains apparently unaltered in all the analyzed regions, even when the LIPSS are fully formed. It is suggested that the important increase of defects in the grains of this transitional band, which also features a nanoscale rough topography on the surface, has an important influence on the superconducting properties, resulting in a decrease of T_c and J_c values (in the low magnetic field range used in MOI experiments).

6. Conclusions

The possibility of arbitrarily steering the penetration of magnetic flux in superconducting chips through the control of surface morphology has been demonstrated. Taking advantage of ultrashort laser processing pulse technologies, we have tailored surface domains consisting of oriented groove structures with submicron periodicity on Nb type-II superconducting thin films. By irradiating the samples with femtosecond laser pulses, we have found an expeditious scalable and ecologically friendly physical procedure that enables the formation of metasurfaces useful for diverting, guiding or parceling magnetic flux with density in the range of millitesla. Our main findings are:

- The orientation of surface ripples (LIPSS, type LSFL) within a given domain produces an anisotropic magnetic field penetration.

In our case, the critical current density along the ripples is enhanced by a factor $\Gamma = 3$, as compared to the perpendicular flow. This factor is obtained experimentally by comparing the field penetration parallel/perpendicular to the arms of the cross structure in Fig. 3, as further detailed in the Supplementary Information (Fig. S9) and has been used as a simulation parameter permitting to reproduce the experimental flux penetration landscapes in a wide range of experimental conditions. As the physical counterpart, magnetic flux becomes trapped in the valleys. Pictorially speaking, flux tubes as well as supercurrents are guided along the grooves of the ripples, acting as rails, and are restrained for perpendicular displacements.

- The boundaries between neighboring LIPSS orientation domains as well as those between them and the adjoining pristine areas play a major role in the penetration of magnetic flux. As shown in Figs. 5 and 6, precise switching of the magnetic flux penetration is achieved by defining neat flanks around the flux path as well as between orientation domains in the targeted flux protected areas. However, fuzzy transition zones in the internal boundaries between the domains act as magnetic flux scatterers, since the flux easily glides along these zones, eventually spreading in the direction of the closest ripple structures.
- Alternating field operation has been tested and increases robustness against imperfections in the focused topography. It is also remarkable that stable and tunable flux packets within the flux pathway are obtained by taking advantage of the flux pinning property, together with the flanking barrier effects.

In order to achieve the targeted surface morphology, some critical processing parameters in the laser treatment must be considered:

- The irradiation conditions must be adjusted in a typically large spot overlap of adjacent laser irradiations so that to ensure the material reconfiguration induced by the selective energy deposition [35]. This implies a trial and error material-dependent process ending up with a set of parameters (laser power, pulse repetition frequency, scanning speed and overlapping between different scan lines). Optimized values are given in the Methods section.
- Magnetic flux hosing effects are improved by a combination of enhanced superconductivity in the LIPSS domains and reduced parameters in the boundaries with untreated zones. This (initially unwanted) effect relates to the material nanostructure induced at the end points of the laser beam scanning lines. In these zones, we have observed an increased number of defects, disorder, a noticeably higher resistivity at room temperature, and a clearly decreased superconducting critical temperatures T_c as deduced from TEM, AFM and MOI local probes, respectively. This picture is also consistent with a reduced critical current density J_c for consistency with numerical simulations of the overall flux penetration features.
- The neat transition across the boundaries between orientational LIPSS domains is crucial to allow supercurrent percolation and flux expulsion within the protected areas. For this purpose, a subtle combination of laser scanning conditions is necessary, compromising the local energy profile of the beam and the superposition of successive laser pulses over a given area. Well-defined laser-patterned domain boundaries require good overlapping among laser scans in different directions. At the same time, care must be taken so as to avoid overtreatment, that ends up with holes in the Nb film, and as a consequence with unwanted flux penetration.

Finally, we recall that this fast (mm^2/min) and scalable laser assisted technology for tailoring thin films surfaces with selective magnetic field penetration may find applications in several fields such as the enhanced shielding of superconducting chips by framing the protected area with a band of LIPSS parallel to the surface, the functionalization of monolithic superconducting metamaterials, vortex diodes, guides, etc or even the accomplishment of tunable superconducting/magnetic hybrid structures [46], which may find application in superconducting microelectronics.

CRediT authorship contribution statement

Elena Martínez: Writing – review & editing, Visualization, Methodology, Investigation, Formal analysis, Data curation, Conceptualization. **Nicolas Lejeune:** Writing – review & editing, Visualization, Software, Investigation, Formal analysis, Data curation, Conceptualization. **Javier Frechilla:** Writing – review & editing, Investigation, Data curation. **Luis Porta-Velilla:** Writing – review & editing, Investigation, Data curation. **Emile Fourneau:** Writing – review & editing, Investigation, Data curation. **Luis A. Angurel:** Writing – review & editing, Supervision, Investigation, Funding acquisition, Conceptualization. **Germán F. de la Fuente:** Writing – review & editing, Investigation, Funding acquisition, Conceptualization. **Jörn Bonse:** Writing – review & editing, Software, Investigation, Formal analysis. **Alejandro V. Silhanek:** Writing – review & editing, Supervision, Methodology, Funding acquisition, Formal analysis, Conceptualization. **Antonio Badía-Majós:** Writing – review & editing, Writing – original draft, Visualization, Supervision, Software, Investigation, Formal analysis, Data curation, Conceptualization.

Declaration of competing interest

The authors declare that they have no known competing financial interests or personal relationships that could have appeared to influence the work reported in this paper.

Data availability

The data of our research is available through a public repository as indicated in the main text (https://doi.org/10.5281/zenodo.11521075).

Acknowledgments

Financial support from Spanish MCIN/AEI/10.13039/501100011033 (project PID2020-113034RB-I00), Gobierno de Aragón (research group T54-23R), Belgian FNRS Fonds de la Recherche Scientifique (project O.0028.22 and PDR T.0204.21), and Hi-Scale COST action (CA19108) are to be ackowledged. N. L. acknowledges support from FRS-FNRS (Research Fellowships FRIA). J. F. and L. P.-V. acknowledge support from Gobierno de Aragón, Spain through the predoctoral contracts programme. The authors also would like to acknowledge the use of Servicio General de Apoyo a la Investigación-SAI and Laboratorio de Microscopías Avanzadas, Universidad de Zaragoza.

Appendix A. Supplementary data

Supplemental Information concerning the microstructural studies on the laser patterned Nb films is provided. This includes theoretical considerations about the formation of LIPSS in Nb, and complementary SEM and AFM characterization. In addition it includes experimental information about the magnetic properties of the laser patterned Nb thin films: AC susceptibility data and additional MOI results that display the local magnetic response of the films under different cycles of applied field.

Supplementary material related to this article can be found online at https://doi.org/10.1016/j.apsusc.2024.161214.

References

[1] J. Clarke, F.K. Wilhelm, Superconducting quantum bits, Nature 453 (2008) 1031–1042.
[2] C. Granata, A. Vettoliere, Nano superconducting quantum interference device: A powerful tool for nanoscale investigations, Phys. Rep. 614 (2016) 1–69.
[3] A. Imre, G. Csaba, L. Ji, A. Orlov, G.H. Bernstein, W. Porod, Majority logic gate for magnetic quantum-dot cellular automata, Science 311 (2006) 205–208.
[4] D.B. Carlton, N.C. Emley, E. Tuchfeld, J. Bokor, Simulation studies of nanomagnet-based logic architecture, Nano Lett. 8 (2008) 4173–4178.
[5] A.M. Kadin, Duality and fluxonics in superconducting devices, J. Appl. Phys. 68 (1990) 5741–5749.
[6] J.E. Villegas, S. Savel'ev, F. Nori, E.M. González, J.V. Anguita, R. García, J.L. Vicent, A superconducting reversible rectifier that controls the motion of magnetic flux quanta, Science 302 (2003) 1188–1191.
[7] O.V. Dobrovolskiy, M. Huth, Dual cut-off direct current-tunable microwave low-pass filter on superconducting Nb microstrips with asymmetric nanogrooves, Appl. Phys. Lett. 106 (2015) 142601.
[8] V.K. Vlasko-Vlasov, F. Colauto, T. Benseman, D. Rosenmann, W.K. Kwok, Triode for magnetic flux quanta, Sci. Rep. 6 (2016/11/15) 36847.
[9] M. Tinkham, Introduction to superconductivity, in: International Series in Pure and Applied Physics, McGraw Hill, 1996.
[10] A. Megrant, C. Neill, R. Barends, B. Chiaro, Y. Chen, L. Feigl, J. Kelly, E. Lucero, M. Mariantoni, P.J.J. O'Malley, D. Sank, A. Vainsencher, J. Wenner, T.C. White, Y. Yin, J. Zhao, C.J. Palmstrøm, J.M. Martinis, A.N. Cleland, Planar superconducting resonators with internal quality factors above one million, Appl. Phys. Lett. 100 (2012) 113510.
[11] L. Nulens, N. Lejeune, J. Caeyers, S. Marinković, I. Cools, H. Dausy, S. Basov, B. Raes, M.J. Van Bael, A. Geresdi, A.V. Silhanek, J. Van de Vondel, Catastrophic magnetic flux avalanches in NbTiN superconducting resonators, Commun. Phys. 6 (2023/09/22) 267.
[12] A.K. Niessen, J. Van Suchtelen, F.A. Staas, W.F. Druyvesteyn, Guided motion of vortices and anisotropic resistivity in type-II superconductors, Philips Res. Rep. 20 (1965) 226–234.
[13] D.D. Morrison, R.M. Rose, Controlled pinning in superconducting foils by surface microgrooves, Phys. Rev. Lett. 25 (1970) 356–359.
[14] O. Daldini, P. Martinoli, J.L. Olsen, G. Berner, Vortex-line pinning by thickness modulation of superconducting films, Phys. Rev. Lett. 32 (1974) 218–221.
[15] O.K. Soroka, V.A. Shklovskij, M. Huth, Guiding of vortices under competing isotropic and anisotropic pinning conditions: Theory and experiment, Phys. Rev. B 76 (2007) 014504.
[16] J. Albrecht, A.T. Matveev, J. Strempfer, H.-U. Habermeier, D.V. Shantsev, Y.M. Galperin, T.H. Johansen, Dramatic role of critical current anisotropy on flux avalanches in MgB_2 films, Phys. Rev. Lett. 98 (2007) 117001.
[17] B. Oripov, T. Bieler, G. Ciovati, S. Calatroni, P. Dhakal, T. Junginger, O.B. Malyshev, G. Terenziani, A.-M. Valente-Feliciano, R. Valizadeh, S. Wilde, S.M. Anlage, High-frequency nonlinear response of superconducting cavity-grade Nb surfaces, Phys. Rev. Appl. 11 (2019) 064030.
[18] A.V. Emelianov, M. Pettersson, I.I. Bobrinetskiy, Ultrafast laser processing of 2D materials: Novel routes to advanced devices, Adv. Mater. (2024) 2402907.
[19] M. Birnbaum, Semiconductor surface damage produced by ruby lasers, J. Appl. Phys. 36 (1965) 3688–3689.
[20] H.M. van Driel, J.E. Sipe, J.F. Young, Laser-induced periodic surface structure on solids: A universal phenomenon, Phys. Rev. Lett. 49 (1982) 1955–1958.
[21] J. Bonse, S. Gräf, Maxwell meets Marangoni—A review of theories on laser-induced periodic surface structures, Laser Photonics Rev. 14 (2020) 2000215.
[22] J. Bonse, S. Höhm, S.V. Kirner, A. Rosenfeld, J. Krüger, Laser-induced periodic surface structures— A scientific evergreen, IEEE J. Sel. Top. Quantum Electron. 23 (2017) 9000615.
[23] J. Bonse, Quo vadis LIPSS?—Recent and future trends on laser-induced periodic surface structures, Nanomaterials 10 (2020) 1950.
[24] A. Siegman, P. Fauchet, Stimulated Wood's anomalies on laser-illuminated surfaces, IEEE J. Quantum Electron. 22 (1986) 1384–1403.
[25] A. Rudenko, A. Abou-Saleh, F. Pigeon, C. Mauclair, F. Garrelie, R. Stoian, J.P. Colombier, High-frequency periodic patterns driven by non-radiative fields coupled with Marangoni convection instabilities on laser-excited metal surfaces, Acta Mater. 194 (2020) 93–105.
[26] L. Porta-Velilla, N. Turan, A. Cubero, W. Shao, H. Li, G.F. de la Fuente, E. Martínez, A. Larrea, M. Castro, H. Koralay, S. Cavdar, J. Bonse, L.A. Angurel, Highly regular hexagonally-arranged nanostructures on Ni-W alloy tapes upon irradiation with ultrashort UV laser pulses, Nanomaterials 12 (2022) 2380.
[27] G. Perrakis, O. Tsilipakos, G.D. Tsibidis, E. Stratakis, Impact of hybrid electromagnetic surface modes on the formation of low spatial frequency LIPSS: A universal approach, Laser Photonics Rev. 18 (2024) 2301090.
[28] J. Bonse, K. Sokolowski-Tinten, Probing laser-driven structure formation at extreme scales in space and time, Laser Photonics Rev. 18 (2024) 2300912.
[29] A. Nakhoul, J.-P. Colombier, Beyond the microscale: Advances in surface nanopatterning by laser-driven self-organization, Laser Photonics Rev. 18 (2024) 2300991.
[30] P.M. Fauchet, A.E. Siegman, Surface ripples on silicon and gallium arsenide under picosecond laser illumination, Appl. Phys. Lett. 40 (1982) 824–826.
[31] A. Pan, A. Dias, M. Gomez-Aranzadi, S.M. Olaizola, A. Rodriguez, Formation of laser-induced periodic surface structures on niobium by femtosecond laser irradiation, J. Appl. Phys. 115 (2014) 173101.
[32] A. Cubero, E. Martínez, L.A. Angurel, G.F. de la Fuente, R. Navarro, H. Legall, J. Krüger, J. Bonse, Surface superconductivity changes of niobium sheets by femtosecond laser-induced periodic nanostructures, Nanomaterials 10 (2020) 2525.
[33] C. Kunz, J. Bonse, D. Spaltmann, C. Neumann, A. Turchanin, J.F. Bartolomé, F.A. Müller, S. Gräf, Tribological performance of metal-reinforced ceramic composites selectively structured with femtosecond laser-induced periodic surface structures, Appl. Surf. Sci. 499 (2020) 143917.
[34] A. Cubero, E. Martínez, L.A. Angurel, G.F. de la Fuente, R. Navarro, H. Legall, J. Krüger, J. Bonse, Effects of laser-induced periodic surface structures on the superconducting properties of Niobium, Appl. Surf. Sci. 508 (2020) 145140.
[35] A. Badía-Majós, E. Martínez, L.A. Angurel, G.F. de la Fuente, E. Fourneau, S. Marinković, A.V. Silhanek, Laser nanostructured metasurfaces in Nb superconducting thin films, Appl. Surf. Sci. 649 (2024) 159164.
[36] C.P. Bean, Magnetization of hard superconductors, Phys. Rev. Lett. 8 (1962) 250–253.
[37] C.P. Bean, Magnetization of high-field superconductors, Rev. Modern Phys. 36 (1964) 31–39.
[38] A.R. de la Cruz, R. Lahoz, J. Siegel, G.F. de la Fuente, J. Solis, High speed inscription of uniform, large-area laser-induced periodic surface structures in Cr films using a high repetition rate fs laser, Opt. Lett. 39 (8) (2014) 2491–2494.
[39] G. Shaw, J. Brisbois, L.B.G.L. Pinheiro, J. Müller, S. Blanco Alvarez, T. Devillers, N.M. Dempsey, J.E. Scheerder, J. Van de Vondel, S. Melinte, P. Vanderbemden, M. Motta, W.A. Ortiz, K. Hasselbach, R.B.G. Kramer, A.V. Silhanek, Quantitative magneto-optical investigation of superconductor/ferromagnet hybrid structures, Rev. Sci. Instrum. 89 (2018) 023705.
[40] E.H. Brandt, Geometric barrier and current string in type-II superconductors obtained from continuum electrodynamics, Phys. Rev. B 59 (1999) 3369–3372.
[41] L. Prigozhin, Solution of thin film magnetization problems in type-II superconductivity, J. Comput. Phys. 144 (1998) 180–193.
[42] E.H. Brandt, Square and rectangular thin superconductors in a transverse magnetic field, Phys. Rev. Lett. 74 (1995) 3025–3028.
[43] A. Badía-Majós, C. López, Electromagnetics close beyond the critical state: thermodynamic prospect, Supercond. Sci. Technol. 25 (10) (2012) 104004.
[44] C. Jooss, R. Warthmann, A. Forkl, H. Kronmüller, High-resolution magneto-optical imaging of critical currents in $YBa_2Cu_3O_{7-\delta}$ thin films, Physica C 299 (1998) 215–230.
[45] F. Colauto, M. Motta, W.A. Ortiz, Controlling magnetic flux penetration in low-T_c superconducting films and hybrids, Supercond. Sci. Technol. 34 (2020) 013002.
[46] V.K. Vlasko-Vlasov, F. Colauto, A.I. Buzdin, D. Rosenmann, T. Benseman, W.-K. Kwok, Magnetic gates and guides for superconducting vortices, Phys. Rev. B 95 (2017) 144504.